Single-Cycle Nonlinear Optics

E. Goulielmakis,[1]* M. Schultze,[1] M. Hofstetter,[2] V. S. Yakovlev,[2] J. Gagnon,[1]
M. Uiberacker,[2] A. L. Aquila,[3] E. M. Gullikson,[3] D. T. Attwood,[3] R. Kienberger,[1]
F. Krausz,[1,2]* U. Kleineberg[2]*

Nonlinear optics plays a central role in the advancement of optical science and laser-based technologies. We report on the confinement of the nonlinear interaction of light with matter to a single wave cycle and demonstrate its utility for time-resolved and strong-field science. The electric field of 3.3-femtosecond, 0.72-micron laser pulses with a controlled and measured waveform ionizes atoms near the crests of the central wave cycle, with ionization being virtually switched off outside this interval. Isolated sub-100-attosecond pulses of extreme ultraviolet light (photon energy ~ 80 electron volts), containing ~0.5 nanojoule of energy, emerge from the interaction with a conversion efficiency of ~10^{-6}. These tools enable the study of the precision control of electron motion with light fields and electron-electron interactions with a resolution approaching the atomic unit of time (~24 attoseconds).

Nonlinear electron-light interactions driven by strong light fields of controlled waveform (1) have allowed for the control of electronic motion at light frequencies and the real-time observation of electron dynamics inside and between atoms with ~100-as resolution (2–7). However, time-domain access to a number of fundamental processes, such as the intra-atomic energy transfer between electrons (resulting, for example, in shake-up) (8), the response of an atomic electron system to external influence (e.g., to ionizing radiation) (9) and its rearrangement after the sudden loss of one or more electrons

(10), the charge transfer in biologically relevant molecules (11) and related changes in chemical reactivity (12) or because of nonadiabatic tunneling (13, 14), would require (or benefit from) an improved temporal resolution.

We used waveform-controlled sub-1.5-cycle near-infrared (NIR) light to demonstrate the generation of robust, energetic, isolated sub-100-as pulses of extreme ultraviolet (XUV) radiation and their precise temporal characterization. Photo-ionization confined to a single wave cycle results in observables (such as high-harmonic photons and electrons emitted by above-threshold ioniza-

tion) that can now be related to several distinguishable subcycle ionization events and subsequent electron trajectories with a known timing with respect to the driving field, whose strength and temporal evolution is accurately known (3). These circumstances provide ideal conditions for testing models of strong-field control of electron motion and electron-electron interactions.

The generation of attosecond pulses benefits from the abrupt onset of ionization within a single half-cycle, which minimizes the density of free electrons and, hence, the distortion of the driving wave and its dephasing with the generated harmonic wave. As a result, the coherent build-up of the harmonic emission over an extended propagation is maximized. In addition, the order-of-magnitude variation of the ionization probability between adjacent half-cycles creates unique conditions for single sub-100-as pulse emission without the need for sophisticated gating techniques (5, 15, 16).

On the measurement side, improved resolution results from three provisions: (i) shorter

[1]Max-Planck-Institut für Quantenoptik, Hans-Kopfermann-Strasse 1, D-85748 Garching, Germany. [2]Department für Physik, Ludwig-Maximilians-Universität, Am Coulombwall 1, D-85748 Garching. [3]Center for X-Ray Optics, Lawrence Berkeley National Laboratory, Berkeley, CA 94720, USA.

*To whom correspondence should be addressed. E-mail: elgo@mpq.mpg.de (E.G.); krausz@lmu.de (F.K.); ulf.kleineberg@physik.uni-muenchen.de (U.K.)

Fig. 1. Simulation of sub-femtosecond XUV emission from neon atoms ionized by a linearly polarized, sub-1.5-cycle, 720-nm laser field. E_0 and $a_L(t)$ are inferred from best agreement between the modeled (17) and measured (Fig. 2) spectra and the streaking spectrogram (Fig. 3), respectively. The laser field liberates electrons near its most intense wave crests. (**A**) Classical trajectories of maximum return energy (left panels) and spectra of emerging XUV emission (right panels) are shown for waveforms consistent with $a_L(t)$ inferred from Fig. 3 (correspondence established by colors and line style). The numbers in (i) to (iii) quantify, in units of 10^{-4}, the ionization probability and, hence, the squared modulus of the amplitude of the electron wave packets launched. This amplitude substantially dictates the intensity of XUV emission upon recollision: Contrast ionization probability in (i) to (iii) with the corresponding emission intensities in (iv) to (vi). The pink "dotted-line" emission is not visible in (v) because of the lower ionization probability (by two orders of magnitude) with respect to that resulting in the purple "solid-line" emission [see (ii)]. The gray dashed-and-dotted lines denote the bandpass used in our experiments (fig. S2). φ = 70° and φ = 135° yield highest contrast [see (B)] and highest XUV cutoff energy, respectively. arb.u., arbitrary units. (**B**) Contrast versus CE phase. Here, contrast is defined as the ratio of the energy of the main attosecond XUV pulse to the overall XUV emission energy transmitted through the bandpass [gray dashed-and-dotted lines in (A)].
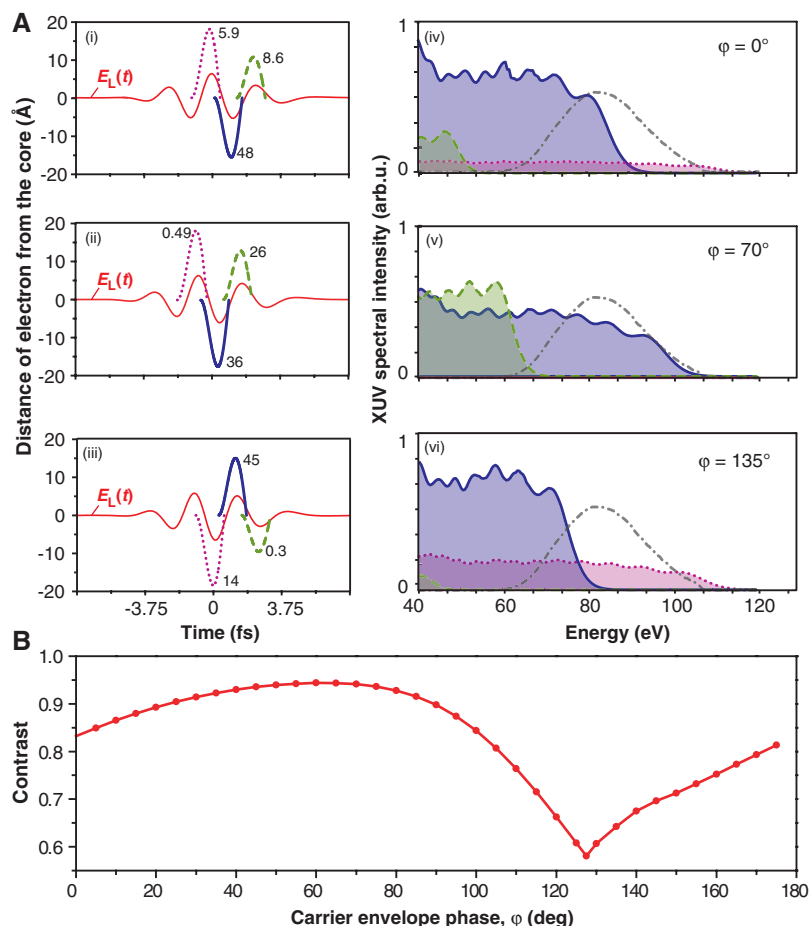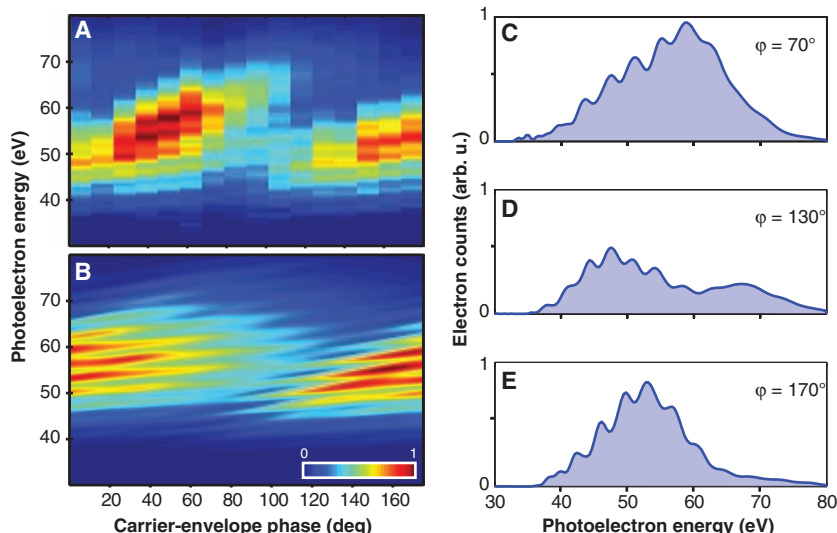
Fig. 2. Control of bandpass-filtered XUV emission with the waveform of monocycle light. Measured (**A**) and simulated (**B**) (*17*) photoelectron spectra versus CE phase, with the delay increased in steps of ~11° ($^{\pi}/_{16}$ rad). (**C** to **E**) Spectra measured at the CE phase setting closest to the values selected in Fig. 1A. The zero of the CE phase scale in (A) was set to yield the best agreement with the modeled spectra in (B).
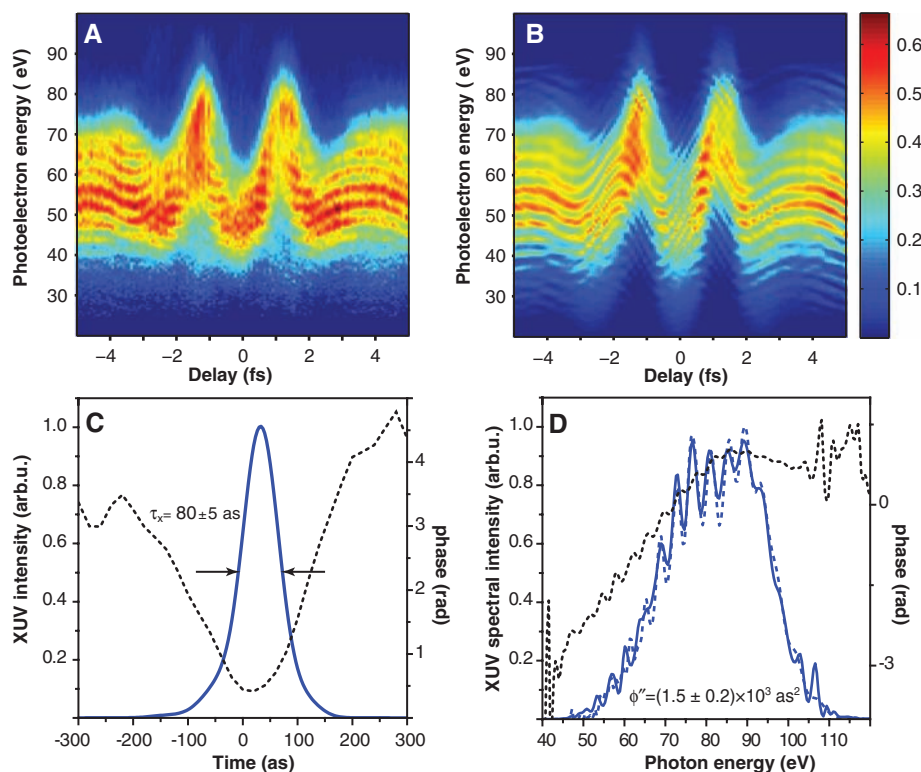

Fig. 3. Sub-100-as XUV pulse retrieval. (**A**) Measured ATR spectrogram compiled from 126 energy spectra of photoelectrons launched by an XUV pulse with a bandwidth of ~28 eV (FWHM) and recorded at delay settings increased in steps of 80 as. Here, a positive delay corresponds to the XUV pulse arriving before the NIR pulse. The high flux of the XUV source allows this spectrogram to be recorded within ~30 min. (**B**) ATR spectrogram reconstructed after ~10^3 iterations of the FROG algorithm (*17*). (**C**) Retrieved temporal intensity profile and spectral phase of the XUV pulse. The intrinsic chirp of the XUV emission (Fig. 4B) is almost fully compensated by a 300-nm-thick Zr foil introduced into the XUV beam between the attosecond source and the ATR measurement. Arrows indicate the temporal FWHM of the XUV pulse. (**D**) XUV spectra evaluated from the measurement of the XUV-generated photoelectron spectrum in the absence of the NIR streaking field (blue dashed line) and from the ATR retrieval (blue solid line). The black dotted line indicates the retrieved spectral phase.

XUV pulse duration, (ii) improved signal-to-noise (S/N) ratio due to the increased XUV photon flux, and (iii) stronger streaking before the onset of the NIR field–induced ionization in attosecond streaking (*2*) or enhanced S/N ratio due to a reduced number of tunneling steps in attosecond tunneling spectroscopy (*14*).

Figure 1 summarizes results of the modeling of the single-cycle interaction of ionizing NIR radiation with an ensemble of neon atoms (*17*). In Fig. 1A, the left panels plot possible NIR electric waveforms, $E_L(t) = E_0 a_L(t) e^{-i(\omega_L t + \varphi)} + cc$ (where *cc* stands for complex conjugate) derived from our streaking measurements (as presented in the next sections) for different settings of the carrier-envelope (CE) phase, φ. Here, E_0 is the peak electric-field strength, $a_L(t)$ is the normalized complex amplitude envelope, and ω_L is the carrier frequency. The probability of ionization outside the central cycle is more than two orders of magnitude lower than that at the field maximum and hence is negligible.

The spectra of XUV emissions originating from the individual recollisions (*18*) are predicted to differ by tens of electron volts in cut-off energy and by up to orders of magnitude in intensity as a consequence of the single-cycle nature of the driving field. The strong variation of emission energies and intensities within a single wave cycle creates ideal conditions for isolated sub-100-as pulse generation. Indeed, filtering radiation with the bandpass depicted by the dashed-and-dotted line is predicted to isolate XUV radiation with more than 90% of its energy delivered in a single attosecond pulse for a range of CE phases as broad as $30° \leq \varphi \leq 90°$ (Fig. 1B). In contrast, with few-cycle-driven harmonic generation resulting in isolated subfemtosecond pulses over only a relatively narrow range of the CE phase near $\varphi \approx 0°$ (*3*), single-cycle excitation appears to permit robust isolated attosecond pulses for a variety of driver waveforms, ranging from near-cosine– to sine-shaped ones, owing to the order-of-magnitude variation of the ionization probability within a single wave cycle.

We used phase-controlled sub-1.5-cycle laser pulses carried at a wavelength of $\lambda_L = 2\pi c/\omega_L = 720$ nm (*19*) to generate XUV harmonics in a neon gas jet up to photon energies of ~110 eV (fig. S1). The emerging XUV pulse—following a spectral filtering through a bandpass (dashed-and-dotted line in Fig. 1A) introduced by metal foils and a Mo/Si multilayer mirror (fig. S2)—subsequently propagates, along with its NIR driver wave, through a second jet of neon atoms in which the XUV pulse ionizes the atoms in the presence of the NIR field. The freed electrons with initial momenta directed along the electric-field vector of the linearly polarized NIR field are collected and analyzed with time-of-flight spectrometry (*17*).

The variation of the measured photoelectron spectra versus CE phase shows good agreement with the predictions of our simulations (Fig. 2, A and B). Figure 2, C to E, shows plots of electron spectra corresponding to the CE phase

settings selected in Fig. 1A. Apart from a down-shift by the ionization potential of neon (21.5 eV), they reveal close resemblance to the XUV spectra transmitted through the bandpass in Fig. 1A(v), (vi), and (iv), respectively. Figure 2C depicts the broadest filtered spectrum produced by a single recollision [full-line spectrum in Fig. 1A(v)]. Emission from the same recollision dominates also in the spectrum shown in Fig. 2E, with this spectrum red-shifted and (upon transmission through the bandpass) correspondingly narrowed, as predicted in Fig. 1A(iv). The two humps of the spectrum plotted in Fig. 2D are indicative of contributions from two recollisions, in accordance with the "solid-line" and "dotted-line" contributions to the emission spectrum in Fig. 1A(vi).

Before measuring the XUV pulse, we optimized the generation process by "fine-tuning" the NIR laser peak intensity to achieve the broadest possible XUV spectrum transmitted through the bandpass in the range of CE phase settings where the contrast is maximized ($50° – 80°$, according to Fig. 1B) to generate a clean single pulse with the shortest possible duration. For the temporal characterization of the generated XUV supercontinuum, we shined the NIR field into the neon atoms ionized by the XUV pulse to implement the atomic transient recorder (ATR) technique introduced in (2, 3). The NIR field boosts or decreases the momenta of the photoelectrons, depending on their instant of release within the 2.4-fs period of the laser field, resulting in broadened and shifted (streaked) spectra of the electrons' final energy distribution. Figure 3A is a plot of a series of streaked spectra recorded versus delay between the XUV and NIR pulse, which we refer to as an ATR or streaking spectrogram. It is practically equivalent to the spectrogram obtained by frequency-resolved optical gating (FROG) (20), with the oscillating NIR field constituting an attosecond phase gate in the present case (21). As a consequence, a FROG retrieval algorithm (22) allows complete determination of both the (gated) XUV pulse and the (gating) NIR laser field (17). The reconstructed ATR spectrogram is plotted in Fig. 3B and reveals excellent agreement with the measured one.

The retrieved temporal intensity profile and phase of the XUV pulse are shown in Fig. 3C. The pulse duration of $\tau_x = 80 \pm 5$ as is close to its transform limit of 75 as, with a small positive chirp of $\phi'' = (1.5 \pm 0.2) \times 10^3$ as^2 being responsible for the deviation. As a further consistency check of the attosecond pulse retrieval, we compared the measured NIR field–free electron spectrum (dashed blue line in Fig. 3D) with the electron spectrum calculated from the retrieved attosecond pulse (solid line in Fig. 3D). Given that the pulse retrieval draws on streaked spectra that are strongly distorted with respect to the field-free one, the degree of agreement between the retrieved and directly measured spectrum provides yet another conclusive testimony of the reliability of the retrieved data.

The ATR retrieval algorithm indicates the presence of a satellite pulse accompanying the main attosecond pulse, containing ~1% of the energy of the main pulse. This amount of satellite is consistent with the depth of the experimentally observed modulation in the XUV spectrum (Fig. 3D). However, this result is inconsistent with our numerical modeling, which predicts a satellite energy content of some 6 to 7% for the optimum range of CE phase settings (Fig. 1B). From analysis of the streaked spectra recorded at the maximum of the NIR electric field (fig. S3), where the momentum of the electrons released by the main attosecond pulse and its satellite is shifted in opposite directions, we inferred a relative satellite energy of ~8%, which is in good agreement with the prediction of our modeling. As a consequence, the fringe visibility in the XUV spectrum is lower than was implied by the relative amplitude of the satellite pulse. The discrepancy may originate from a temporal jitter between the main pulse and the satellite pulse and/or from a different spatial amplitude distribution of the beams transporting the emission from the adjacent recollision events. The important lesson from these findings is that the fringe visibility in the XUV spectrum does not allow a reliable determination of the

energy carried by the satellite(s) accompanying the main attosecond pulse.

The laser waveform evaluated from the ATR measurement is preserved between the location of the generation and measurement. Figure 4A illustrates the evaluated NIR waveform with electric-field amplitude corresponding to a peak intensity of $I_0 \sim (5.8 \pm 0.5) \times 10^{14}$ W/cm^2, as evaluated from the cut-off of our XUV spectra. The pulse duration [full width at half maximum (FWHM)] of 3.3 fs is in good agreement with the results of previous interferometric autocorrelation measurements (19), and the evaluated CE phase of ~50° is consistent with the optimum contrast according to our modeling (Fig. 1B).

Accurate knowledge of the attosecond XUV pulse parameters, the temporal evolution of the generating NIR field, and the emergence of the former from a single recollision permit one to perform precision tests of models of light-electron interactions underlying the ionization and subsequent attosecond pulse generation processes. As an example, we calculated the intrinsic spectral chirp (i.e., the variation of the group delay versus frequency) carried by the attosecond XUV pulse during its emergence from the chirp measured by the ATR and the known dispersion of the components traversed by the pulse on its way
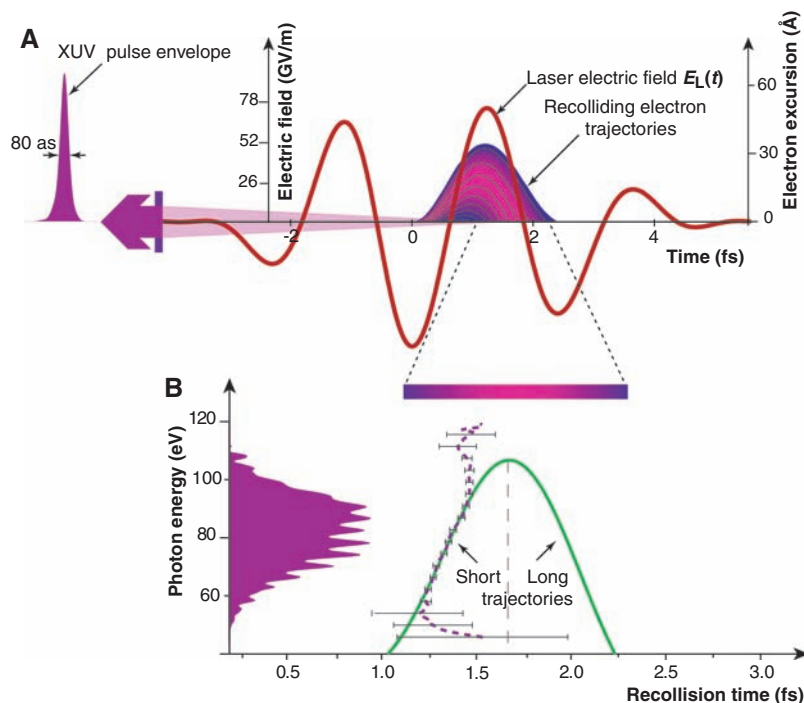

Fig. 4. (**A**) Retrieved electric field of the NIR laser pulse used for generating and measuring the attosecond XUV pulse shown in Fig. 3. The duration of the pulse (FWHM of the cycle-averaged intensity profile) is $\tau_L = 3.3$ fs, and the CE phase is evaluated as $\varphi \sim 50°$. The classical electron trajectories responsible for the emission of the filtered attosecond pulse are calculated with the plotted electric field and shown in the same panel. The color coding indicates the final return energy of the electrons. (**B**) Energy of the recolliding electron plus ionization potential (which is equal to the emitted XUV photon energy) versus recollision time evaluated from the classical trajectory analysis (solid green line), and emitted photon energy versus emission time (dashed purple line) inferred from the chirp of the measured attosecond pulse and the dispersion of the metal filter that the attosecond pulse passes through before the measurement. The basic idea for the graphical representation is borrowed from (29). Error bars indicate the uncertainty in the retrieved group delay.

from the source to the measurement (fig. S2). The result (purple dashed line in Fig. 4B) is compared with the intrinsic attosecond chirp (green solid line in Fig. 4B) calculated from a classical trajectory analysis (*23, 24*). There is a notable discrepancy at the high-energy components of the wave packet, possibly because of quantum effects near cutoff. Nevertheless, the agreement with the attochirp resulting from short trajectories is stunning in the main part of the spectrum, where the S/N ratio is excellent. This agreement indicates the powerfulness of semiclassical modeling of strong-field interactions (*25, 26*) and the negligible role of long trajectories in contributing to the XUV radiation in the far field (*27*).

In a similar way, the confinement of interaction between the ionizing field and the atom to a single wave cycle will permit accurate quantitative tests of theories of strong-field ionization. The sub-100-as XUV pulses emerging from the interaction with a flux greater than 10^{11} photons/s—along with their monocycle NIR driver wave—will push the resolution limit of attosecond spectroscopy to the atomic unit of time (~24 as) and allow for the real-time observation of electron correlations, by means of streaking (*6*), tunneling (*14*), or absorption (*28*) spectroscopy.

References and Notes

1. A. Baltuska *et al.*, *Nature* **421**, 611 (2003).
2. R. Kienberger *et al.*, *Nature* **427**, 817 (2004).
3. E. Goulielmakis *et al.*, *Science* **305**, 1267 (2004).
4. M. F. Kling *et al.*, *Science* **312**, 246 (2006).
5. G. Sansone *et al.*, *Science* **314**, 443 (2006).
6. A. L. Cavalieri *et al.*, *Nature* **449**, 1029 (2007).
7. E. Goulielmakis *et al.*, *Science* **317**, 769 (2007).
8. S. Svensson, B. Eriksson, N. Martensson, G. Wendin, U. J. Gelius, *J. Electron Spectrosc. Relat. Phenom.* **47**, 327 (1988).
9. S. X. Hu, L. A. Collins, *Phys. Rev. Lett.* **96**, 073004 (2006).
10. J. Breidbach, L. S. Cederbaum, *Phys. Rev. Lett.* **94**, 033901 (2005).
11. A. I. Kuleff, J. Breidbach, L. S. Cederbaum, *J. Chem. Phys.* **123**, 044111 (2005).
12. F. Remacle, R. D. Levine, *Proc. Natl. Acad. Sci. U.S.A.* **103**, 6793 (2006).
13. G. Yudin, M. Y. Ivanov, *Phys. Rev. A* **64**, 035401 (2001).
14. M. Uiberacker *et al.*, *Nature* **446**, 627 (2007).
15. T. Pfeifer *et al.*, *Phys. Rev. Lett.* **97**, 163901 (2006).
16. Y. Oishi *et al.*, *Opt. Express* **14**, 7230 (2006).
17. See supporting material on *Science* Online.
18. C. A. Haworth *et al.*, *Nature Phys.* **3**, 52 (2007).
19. A. L. Cavalieri *et al.*, *New J. Phys.* **9**, 242 (2007).
20. R. Trebino, D. J. Kane, *J. Opt. Soc. Am. A* **10**, 1101 (1993).
21. Y. Mairesse, F. Quéré, *Phys. Rev. A* **71**, 011401(R) (2005).
22. D. J. Kane, G. Rodriguez, A. J. Taylor, T. S. Clement, *J. Opt. Soc. Am. B* **14**, 935 (1997).
23. P. Salières *et al.*, *Science* **292**, 902 (2001).
24. V. S. Yakovlev, A. Scrinzi, *Phys. Rev. Lett.* **91**, 153901 (2003).
25. P. B. Corkum, *Phys. Rev. Lett.* **71**, 1994 (1993).
26. K. J. Schafer, B. Yang, L. F. DiMauro, K. C. Kulander, *Phys. Rev. Lett.* **70**, 1599 (1993).
27. R. López-Martens *et al.*, *Phys. Rev. Lett.* **94**, 033001 (2005).
28. Z.-H. Loh *et al.*, *Phys. Rev. Lett.* **98**, 143601 (2007).
29. K. Varjú *et al.*, *Laser Phys.* **15**, 888 (2005).
30. Supported by the Max Planck Society and the Deutsche Forschungsgemeinschaft Cluster of Excellence: Munich Centre for Advanced Photonics (www.munich-photonics.de). E.G. acknowledges a Marie-Curie fellowship (MEIF-CT-2005-02440) and a Marie-Curie Reintegration grant (MERG-CT-2007-208643). A.L.A. is supported by the NSF Extreme Ultraviolet Engineering Research Center. R.K. acknowledges support from the Sofia Kovalevskaya award of the Alexander von Humboldt Foundation.

The Formation Conditions of Chondrules and Chondrites

C. M. O'D. Alexander,[1]* J. N. Grossman,[2] D. S. Ebel,[3] F. J. Ciesla[1]

Chondrules, which are roughly millimeter-sized silicate-rich spherules, dominate the most primitive meteorites, the chondrites. They formed as molten droplets and, judging from their abundances in chondrites, are the products of one of the most energetic processes that operated in the early inner solar system. The conditions and mechanism of chondrule formation remain poorly understood. Here we show that the abundance of the volatile element sodium remained relatively constant during chondrule formation. Prevention of the evaporation of sodium requires that chondrules formed in regions with much higher solid densities than predicted by known nebular concentration mechanisms. These regions would probably have been self-gravitating. Our model explains many other chemical characteristics of chondrules and also implies that chondrule and planetesimal formation were linked.

Chondrules make up ~20 to 80 volume % of most chondrites and formed at peak temperatures of ~1700 to 2100 K (*1*). Chondrules in the different chondrite groups have distinct physical and chemical properties (*2*), as well as distinct age ranges (*3*), indicating that they formed in relatively local environments via a process that operated at least periodically between ~1 and 4 million years after the formation of the solar system.

It was long thought that individual chondrules behaved as chemically closed systems during their formation, inheriting their compositions from their precursors (*4, 5*). However, for likely cooling rates of 10 to 1000 K/hour (*1*) and at the low pressures (total pressure $\approx 10^{-6}$ to 10^{-3} bars) of the solar protoplanetary disk (nebula), experiments (*6–8*), natural analogs (*9, 10*), and theoretical calculations (*11, 12*) all show that there should be extensive evaporation of major and minor elements, in the order S > Na, K > Fe > Si > Mg.

Elemental fractionations in chondrules are generally a function of volatility (*4, 5*). If evaporation in the nebula produced the alkali metal and Fe fractionations, the more volatile elements (such as S) should be entirely absent, which they are not. In addition, the fractionated elements should exhibit large and systematic isotopic fractionations, which they do not (*13*).

Here we demonstrate that chondrules did indeed behave as essentially closed systems during melting, at least for elements with volatilities less than or equal to that of Na. We also propose a means of resolving the apparent conflict between this result and experimental and theoretical expectations that chondrules should have suffered considerable evaporation during formation. Our conclusions have implications for mechanisms of dust concentration in the solar nebula, for chondrule formation, and for planetesimal formation.

Chondrules are dominated by olivine [$(Mg,Fe)_2SiO_4$], pyroxene [$(Mg,Fe,Ca)SiO_3$], Fe-Ni metal, and quenched silicate melt (glass). Many of the more volatile elements (such as Na) can diffuse rapidly, particularly in melts and glasses. Therefore, it is possible that volatiles were completely lost when chondrules melted, and reentered the chondrules during cooling or even after solidification. However, Na clinopyroxene/glass ratios show that the Na contents of the final chondrule melts (now glass) had approximately their observed, relatively high abundances at temperatures of ~1600 to 1200 K (*14–16*).

Calculations suggest that chondrule melts could have been stabilized in the nebula by substantially enriching solids (chondrule precursors or other dust) relative to gas (*11, 12*). This also substantially increases the condensation temperatures of even highly volatile elements such as S (*11, 12*). Even in solid-enriched systems, there is an initial phase of evaporation when a chondrule melts, but subsequent chondrule/gas re-equilibration would erase any isotopic fractionations (*12*). If the enrichment of solids is high, little evaporation may be needed to reach chondrule/gas equilibrium, and the behavior of volatile elements during cooling would resemble closed-system behavior. However, even at a high total pressure of 10^{-3} bars, with a solids enrichment of 1000 relative to the solar composition, all the Na would evaporate at near-liquidus temperatures, and substantial recondensation only begins well below 1600 K (*11*). Locally enriching chondrule-sized or smaller solids by 1000 times

[1]Department of Terrestrial Magnetism, Carnegie Institution of Washington, Washington, DC 20015, USA. [2]U.S. Geological Survey, Reston, VA 20192, USA. [3]American Museum of Natural History, New York, NY 10024, USA.

*To whom correspondence should be addressed. E-mail: alexande@dtm.ciw.edu

Science

Single-Cycle Nonlinear Optics

E. Goulielmakis, M. Schultze, M. Hofstetter, V. S. Yakovlev, J. Gagnon, M. Uiberacker, A. L. Aquila, E. M. Gullikson, D. T. Attwood, R. Kienberger, F. Krausz and U. Kleineberg

ARTICLE TOOLS	http://science.sciencemag.org/content/320/5883/1614
SUPPLEMENTARY MATERIALS	http://science.sciencemag.org/content/suppl/2008/06/19/320.5883.1614.DC1
REFERENCES	This article cites 28 articles, 6 of which you can access for free http://science.sciencemag.org/content/320/5883/1614#BIBL
PERMISSIONS	http://www.sciencemag.org/help/reprints-and-permissions

Use of this article is subject to the Terms of Service